Thermally Forced Gravity Waves in an Atmosphere at Rest

MELVILLE E. NICHOLLS, ROGER A. PIELKE AND WILLIAM R. COTTON

Department of Atmospheric Science, Colorado State University, Fort Collins, Colorado

(Manuscript received 17 September 1990, in final form 11 March 1991)

ABSTRACT

The transient linear response of a quiescent, two-dimensional, nonrotating atmosphere to prescribed heat sources and sinks is investigated. Analytical solutions of the hydrostatic Boussinesq equations are obtained for a rigid lid and for a semi-infinite region. For the rigid lid solution, vertically trapped gravity waves propagate away from the source with a speed that depends on the Brunt–Väisälä frequency and the vertical wavenumber of the heating. The amplitude of the disturbance field in the region of the forcing approaches a constant value. Two modes are of particular interest: 1) a deep fast-moving mode which is responsible for subsidence warming through the depth of the troposphere; 2) a slower moving mode which corresponds to midlevel inflow and lower- and upper-level outflows. A solution is also obtained for a semi-infinite region. Although gravity wave energy can now propagate upward, the structure of the low-level fields still shows many similarities with the rigid lid solution.

An analytical solution is also obtained for the rigid lid case for a pulse forcing function. This solution shows that when the heating is turned off the disturbance separates into two parts moving in opposite directions. The structure of these propagating disturbances is similar to gravity waves produced in two-dimensional numerical simulations of Florida convection. A term analysis is presented that confirms the predominantly linear character of the numerically simulated gravity waves.

1. Introduction

In this paper, we investigate the linear response of a quiescent atmosphere to heating profiles characteristic of convective and stratiform regions of mesoscale cloud lines. This simple model appears to have relevance to convective lines forming in environments without significant shear and possibly to certain aspects of systems forming in sheared environments. A solution for a heating function, which is turned off at some time, has similarities to gravity waves produced in a simulation of an orogenic convective system (Tripoli and Cotton 1989a,b) and in two-dimensional simulations of Florida convection (Nicholls et al. 1991).

The transient linear response of the atmosphere to prescribed heat sources and sinks has recently been investigated by Lin and Smith (1986), Raymond (1986), and Bretherton (1988). In these studies the basic state is a moving stratified flow. They find that downward motion can develop within the heat source region, which is consistent with observations of flow past "heat islands" (Garstang et al. 1975; Mahrer and Pielke 1976). However, if heating is due to the release of latent heat and condensation occurs because air rises, there may be a constraint that the heating is to a large degree in phase with the vertical velocity in convective systems. Hence, in this study we investigate the simpler situation where the atmosphere is initially motionless relative to the prescribed thermal forcing. This work can be regarded as a special case of Lin and Smith (1986) with no mean flow, who obtained numerical solutions for vertical displacement in the case of a maintained heat source. In this study, analytical solutions are found for the case of a rigid lid and for a semi-infinite region for heating profiles characteristic of both convective and stratiform regions. The analytical linear model gives insight into the structure and evolution of some of the features seen in mesoscale convective lines. Connections are drawn between linear solutions and the gravity waves generated in a numerical simulation of transient convection over the Florida peninsula.

Observational studies of squall lines have shown the presence of a surface mesoscale high with mesoscale lows both to the front and rear of the system (Fujita 1963; Hoxit et al. 1976; Zipser 1977; Johnson and Nicholls 1983; Johnson and Hamilton 1988). LeMone (1983) and LeMone et al. (1984) identified a mesolow approximately 2 km above the surface mesohigh within tropical convective lines. Modeling studies by Nicholls (1987) and Nicholls et al. (1988) have successfully replicated these features of the pressure field. They show that they are associated with significant horizontal velocity perturbations at large distances from the convective region of the squall line. The mesolow that develops above the surface is intimately related to the

Corresponding author address: Dr. Melville E. Nicholls, Dept. of Atmospheric Science, Colorado State University, Fort Collins, CO 80523.

formation of the rear inflow jet, which has been the focus of observational studies (i.e., Smull and Houze 1987). The high pressure at the surface is a consequence of low-level cooling that produces a cold pool. The release of latent heat causes the air above the cold pool to be warmer than the surrounding environment, which hydrostatically accounts for the presence of the mesolow above the surface. Compensating subsidence outside the convective region occurs on either side of the system producing warming and the associated broad surface mesolows. Observational studies of persistent large amplitude gravity waves by Lin and Goff (1988) and Bosart and Simon (1988) suggest that they were initiated by convective systems. Numerical simulations of an orogenic mesoscale convective system by Tripoli and Cotton (1989a,b) and of Florida convection by Nicholls et al. (1991) produced deep rapidly moving gravity waves as the systems decayed in intensity. The goal of this investigation is to explain using a simple model how some of these features develop and evolve.

The model presented in this paper is idealized. The solution, found for a quiescent environment and particular prescribed heating functions to be described later, takes the form of a symmetrical disturbance propagating away from the heat source. Intense squall lines, on the other hand, typically have a pronounced asymmetry since the updraft flows from front-to-rear and the downdraft from rear-to-front. The importance of shear for the development of intense squall lines has been emphasized by Hane (1973), Thorpe et al. (1982), Rotunno et al. (1988), Nicholls et al. (1988), and Schmidt and Cotton (1990). There are, however, instances when convective lines form in environments without appreciable shear; for example, the slow moving tropical cloud lines studied by Barnes and Sieckman (1984) and the majority of Florida convective lines (Blanchard and Lopez 1985). Furthermore, in the numerical modeling studies by Thorpe et al. (1982), Dudhia et al. (1987), Rotunno et al. (1988), and Nicholls et al. (1988), environments were considered that had strong low-level shear, but throughout most of the troposphere shear was absent or weak. In some cases the interaction of the cold pool with the low-level shear produced a vertically oriented jet, which fed deep convective cells that were stationary with respect to the quiescent environment aloft. The model presented in this paper may have some relevance to the compensating subsidence outside the convective region for this case. Even for complicated environmental wind profiles a symmetrical response can at times be found, such as in the simulation by Nicholls (1987) of a tropical squall line that developed in a low-level jet. In the early stages of development a pronounced symmetrical response was evident, especially exterior to the convective region. (Figs. 17, 18, and 19 of that paper).

Within the convective region, the linear and hydrostatic assumptions are clearly violated. Although the focus of this study is on the circulation outside the convective region for which these approximations are more reasonable, the relevance of a solution that neglects the nonhydrostatic and nonlinear effects within the region of large latent heat release is certainly questionable. It appears that to some extent the linear hydrostatic solution has similarities with the fields of observed and numerically simulated systems, especially exterior to the convective region. Even in the convective region some of the broad characteristics of the linear hydrostatic solution are retained. A linear nonhydrostatic model of a supercell storm (Lin and Li 1988) also appears to replicate some of the features of a highly nonlinear system. Within stratiform regions the linear and hydrostatic approximations are more reasonable. We present a term analysis for the gravity wave produced in a two-dimensional numerical simulation of Florida convection, which shows that it is predominantly linear in character, even though within the convective region nonlinearities are significant.

The heating profiles used in this study are based on results of Houze (1982) and Johnson and Young (1983) who emphasize the differences that exist between convective and stratiform regions. They find that for convective regions of tropical mesoscale systems the heating profile has warming at all levels with a maximum at midlevels, whereas in stratiform regions there is a warming peak in the upper troposphere and a cooling peak at low-levels. In this study, we do not attempt to use a spatially distributed heat source having the characteristics of a narrow convective region with a larger trailing stratiform region, which is often the case for squall lines, but instead look at the response to these individual components.

In section 2, an analytical solution is derived for a rigid lid. In section 3, we extend these results by obtaining a solution for a semi-infinite region. In section 4, an analytical solution is found for a pulsed heating function. In section 5, a term analysis is presented for a gravity wave produced in a two-dimensional simulation of Florida convection.

2. Solution for a rigid lid

The two-dimensional incompressible hydrostatic Boussinesq equations are

$$\frac{\partial u}{\partial t} + \frac{1}{\rho_0}\frac{\partial p'}{\partial x} = 0 \tag{1}$$

$$\frac{1}{\rho_0}\frac{\partial p'}{\partial z} = b \tag{2}$$

$$\frac{\partial b}{\partial t} + wN^2 = Q \tag{3}$$

$$\frac{\partial u}{\partial x} + \frac{\partial w}{\partial z} = 0, \tag{4}$$

where u, w are the velocities, p' is the perturbation pressure, b is the buoyancy, N is the buoyancy frequency per mass unit, and $Q = gQ_m/c_pT$ is the thermal forcing with Q_m the heating rate per unit mass. For subsequent derivations the prime on p is dropped. For ρ_0 constant, these equations can be manipulated to obtain an equation for the perturbation pressure,

$$\frac{\partial^2}{\partial t^2} p_{zz} + N^2 p_{xx} = \frac{\partial}{\partial t}\frac{\partial}{\partial z}(\rho_0 Q). \tag{5}$$

For this solution we set ρ_0 to a constant equal to 1 kg m^{-3}. The form of the thermal forcing used is

$$Q = Q_0\left(\frac{a^2}{x^2 + a^2}\right)\sin(lz), \tag{6}$$

where Q_0 is the magnitude of the thermal forcing, a is the half-width, and $l = n\pi/H$ is the vertical wavenumber of the heating between $z = 0$ and $z = H$. The magnitude of the heating rate is $Q_{m0} = Q_0 c_p T/g$ J kg^{-1} s^{-1} (when values of Q_{m0} are given it will be for an assumed value of $T = 273$ K). Since the heating is not a function of time, the rhs of Eq. (5) is zero. Taking the Fourier and Laplace transforms of Eq. (5) we obtain

$$s^2\hat{p}_{zz} - \frac{\partial}{\partial t}\tilde{p}_{zz}(t = 0) - k^2N^2\hat{p} = 0, \tag{7}$$

where $\tilde{(\ )}$ indicates the Fourier transform and $\hat{(\ )}$ indicates that both the Fourier and Laplace transforms have been taken. From Eqs. (2) and (3) we find

$$\frac{\partial}{\partial t} p_{zz}(t = 0) = Q_z. \tag{8}$$

Therefore, Eq. (7) becomes

$$\hat{p}_{zz} - \lambda^2\hat{p} = \frac{Q_0 a e^{-ak}}{s^2} l\cos(lz), \tag{9}$$

where $\lambda = kN/s$. From Eqs. (2), (3), and (6) the appropriate boundary condition at $z = 0$ and $z = H$, the height of the rigid lid, is $\partial\hat{p}/\partial z = 0$. The solution to Eq. (9) is found to be

$$\hat{p} = -\frac{Q_0 a e^{-ak}\cos(lz)}{l[s^2 + (kN/l)^2]}. \tag{10}$$

The inverse Laplace transform gives

$$\tilde{p} = -\frac{Q_0 a e^{-ak}}{kN}\cos(lz)\sin\left(\frac{kNt}{l}\right). \tag{11}$$

Taking the inverse Fourier transform and using Eqs. (1)–(4) to derive the other variables, the following equations are obtained:

$$p(x, z, t) = -\frac{Q_0 a\cos(lz)}{N}\cdot\frac{1}{2}\left[\tan^{-1}\left(\frac{Nt/l + x}{a}\right) + \tan^{-1}\left(\frac{Nt/l - x}{a}\right)\right] \tag{12}$$

$$b(x, z, t) = \frac{Q_0 a l\sin(lz)}{N}\cdot\frac{1}{2}\left[\tan^{-1}\left(\frac{Nt/l + x}{a}\right) + \tan^{-1}\left(\frac{Nt/l - x}{a}\right)\right] \tag{13}$$

$$w(x, z, t) = \frac{Q_0\sin(lz)}{N^2}\left\{\frac{a^2}{x^2 + a^2} - \frac{1}{2}\left[\frac{1}{1 + \left(\frac{Nt/l + x}{a}\right)^2} + \frac{1}{1 + \left(\frac{Nt/l - x}{a}\right)^2}\right]\right\} \tag{14}$$

$$u(x, z, t) = \frac{Q_0 a l\cos(lz)}{N^2}\cdot\frac{1}{2}\left\{\tan^{-1}\left(\frac{Nt/l + x}{a}\right) - \tan^{-1}\left(\frac{Nt/l - x}{a}\right) - 2\tan^{-1}\left(\frac{x}{a}\right)\right\}. \tag{15}$$

The solution can also be derived for a forcing that is switched on at $t = T$, thus having the form of a step function. The solution is identical except translated in time and becomes exactly identical when $T = 0$. The solution for the perturbation pressure [Eq. (12)] is comprised of two waves moving in opposite directions. The arctangent form of these two waves [i.e., bracketed term in Eq. (12)] is shown in Figs. 1a and 1b. Initially the arctangent curves sum to give zero. At a later time the curves have moved in opposite directions and sum to give a net perturbation shown by the dashed line in Fig. 1b. The negative of this curve shows how the surface pressure field evolves in response to warming (Q_0

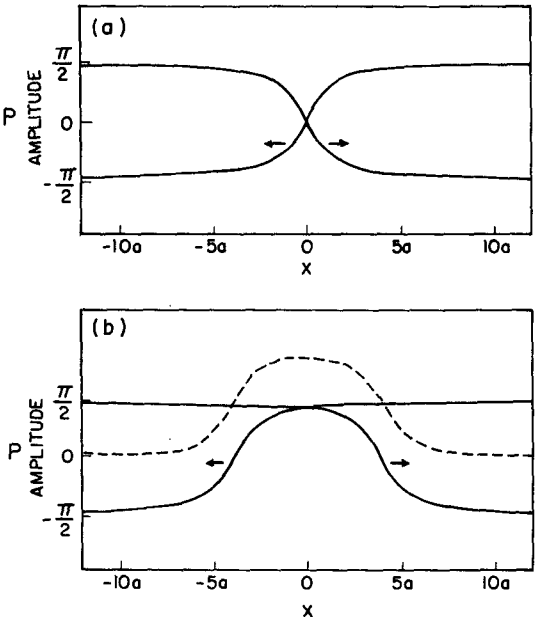

FIG. 1. Arctangent curves: (a) initially; (b) later. The dashed curve shows the summation of the two waves.

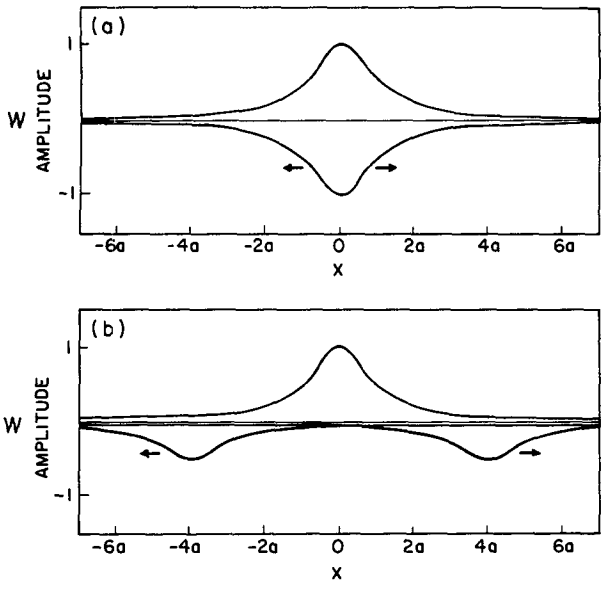

FIG. 2. Solution for vertical velocity: (a) initially; (b) later.

positive, $n = 1$). The equation for vertical velocity is a little different. Figures 2a and 2b show that initially the upper curve $a^2/(x^2 + a^2)$ is negated by the sum of two lower curves. These lower curves move in opposite directions leaving upward motion in the center if $Q_0 \sin(lz)$ is positive. The scale of the moving subsident regions depends on a, the half-width of the heating function. The amplitude is directly proportional to the heating rate and inversely proportional to N^2. These two outgoing waves have also been found in the studies by Lin and Smith (1986), Bretherton (1988), and Bretherton and Smolarkiewicz (1989).

The speed of the waves is given by

$$c = \frac{NH}{n\pi}. \tag{16}$$

Hence, the speed at which the waves travel depends on the Brunt–Väisälä frequency and the vertical wavenumber of the forcing. That the speed of internal gravity wave modes depends on their vertical scale is well known and emphasized in an early study of sea-breeze circulations by Geisler and Bretherton (1969). The amplitude of the response approaches a constant value. For instance, Fig. 1 for the horizontal variation of pressure shows that, once the region of the arctangent curve having the largest gradient passes a point, the two curves sum to slowly approach π. The time taken for the amplitude of the response to reach 90% of the maximum value attainable is given approximately by $t \approx 6n\pi a/NH$. For $n = 1$, $a = 10$ km, $N = 0.01$ s^{-1}, and $H = 10$ km, we find $t \approx 0.5$ h. This behavior can also be deduced from the solution for the displacement, determined by Lin and Smith (1986).

Figures 3a–d show fields of u, w, p, and b, respectively, at $t = 2$ h, for $n = 1$ and Q_0 positive. The values of Q_{m0} is 2 J kg^{-1} s^{-1}, which, for $H = 10$ km and $a = 10$ km, gives a net heat input of $2Ha\rho_0 Q_{m0} = 4 \times 10^8$ J s^{-1} m^{-1} (where ρ_0 is taken to be 1 kg m^{-3}). This would correspond to a precipitation rate over a region of width $d = 20$ km of $(4 \times 10^8$ J s^{-1} m^{-1})/$(\rho_w L d) \sim 30$ mm h^{-1}, where ρ_w is the density of water and L is the latent heat of condensation. The heating profile is a half-sine wave in the vertical. Note that since the solution is symmetrical about the $x = 0$ axis, results for this and subsequent figures are only shown for $x > 0$. The horizontal velocity field shows low-level inflow and upper-level outflow. Compensating subsidence outside the updraft leads to deep warming. The

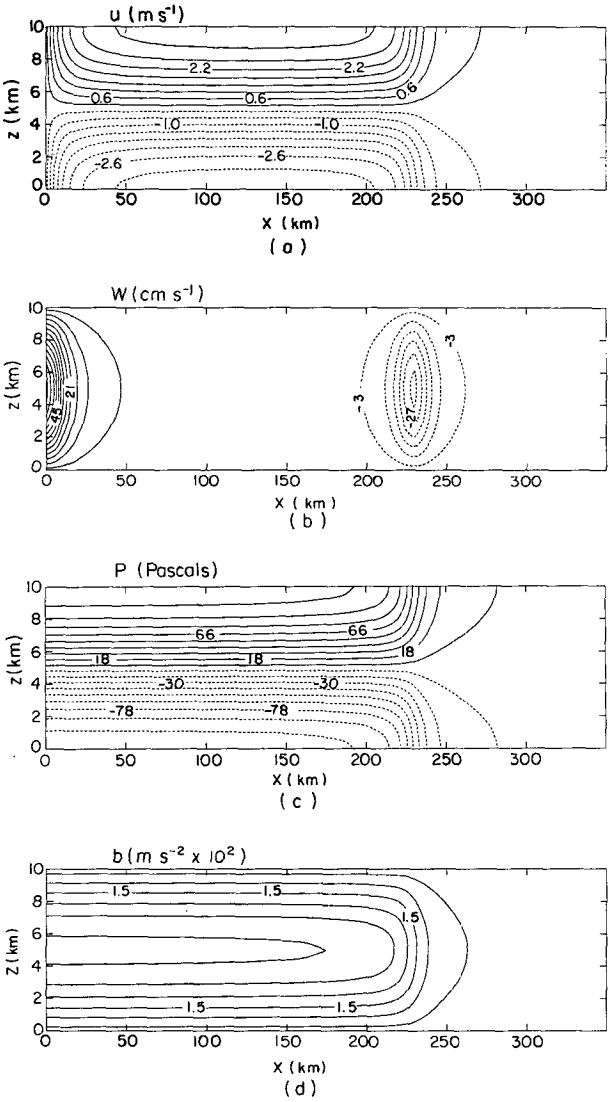

FIG. 3. Rigid-lid solution for the $n = 1$ mode. $Q_{m0} = 2.0$ J kg^{-1} s^{-1}, $a = 10$ km, $H = 10$ km, $N = 0.01$ s^{-1}, and $t = 2$ h. (a) Horizontal velocity. The contour interval is 0.4 m s^{-1}. (b) Vertical velocity. The contour interval is 6 cm s^{-1}. (c) Perturbation pressure. The contour interval is 12 pascals. (d) Perturbation buoyancy. The contour interval is 0.006 m s^{-2}, and the label scale is 100.

pressure perturbation is negative below $H/2$ and symmetrical with a high above $H/2$.

The $n = 2$ mode is not shown, but is easy to picture, since it can be thought of as similar to the $n = 1$ mode but with one full cycle of sinusoidal oscillation in the vertical and one-half the propagation speed [this is discussed by Gill (1980) for a similar type of problem]. For Q_0 negative, the heating function is a sine wave in the vertical with cooling at low levels and warming aloft. Hence, there is midlevel inflow with outflow at upper and lower levels. At $x = 0$, there is upward motion aloft and downward motion below. A low pressure occurs at midlevels with symmetrical highs above and below. The buoyancy perturbation is positive above $H/2$ and negative below.

Cloud lines often consist of a narrow region ~20 km wide of active convection and a larger trailing stratiform region. Johnson and Young (1983) in a study of winter MONEX (International Winter Monsoon Experiment) systems emphasize the differences in the apparent heating profiles (Yanai et al. 1973) between these regions. In the convective region, the heating profile has a warming at all levels with a peak in the midtroposphere. In the stratiform region there is a warming peak in the upper troposphere and a cooling peak at lower levels. The heating profile for the $n = 1$ mode is similar to the situation in the convective region. To obtain a heating profile similar to that found by Johnson and Young (1983, see their Fig. 6) the two modes are superimposed as shown in Fig. 4. Note that sine functions are not capable of representing the weak surface cooling indicated in the observations. These sum to give a region of warming above a weaker low-level cooling. Figures 5a–d show fields of u, w, p and b, respectively, at $t = 2$ h. For each mode $Q_{m0} = 1$ J kg^{-1} s^{-1}. The individual modes are quite apparent. The deep, fast moving $n = 1$ mode produces subsidence warming at large distances from $x = 0$. Associated with this mode is flow towards the source at low levels and away from it aloft, which is evident for large x. The broad surface low is due to this mode. The $n = 2$ mode contributes to upward motion aloft and downward motion at low levels at $x = 0$. It is associated with midlevel inflow and upper- and lower-level outflows. The low-level outflow from the second mode and the low-level inflow from the first mode results in a surface gust front at $x \approx 115$ km.

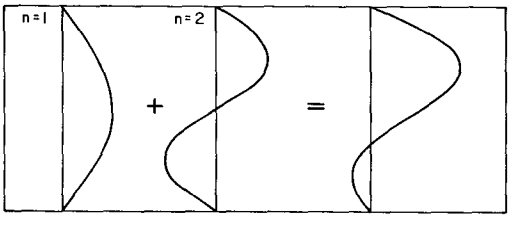

FIG. 4. Vertical distribution of the thermal forcing for $n = 1$ and 2 and their sum. Q_0 is the same magnitude for each mode, positive for $n = 1$, negative for $n = 2$.

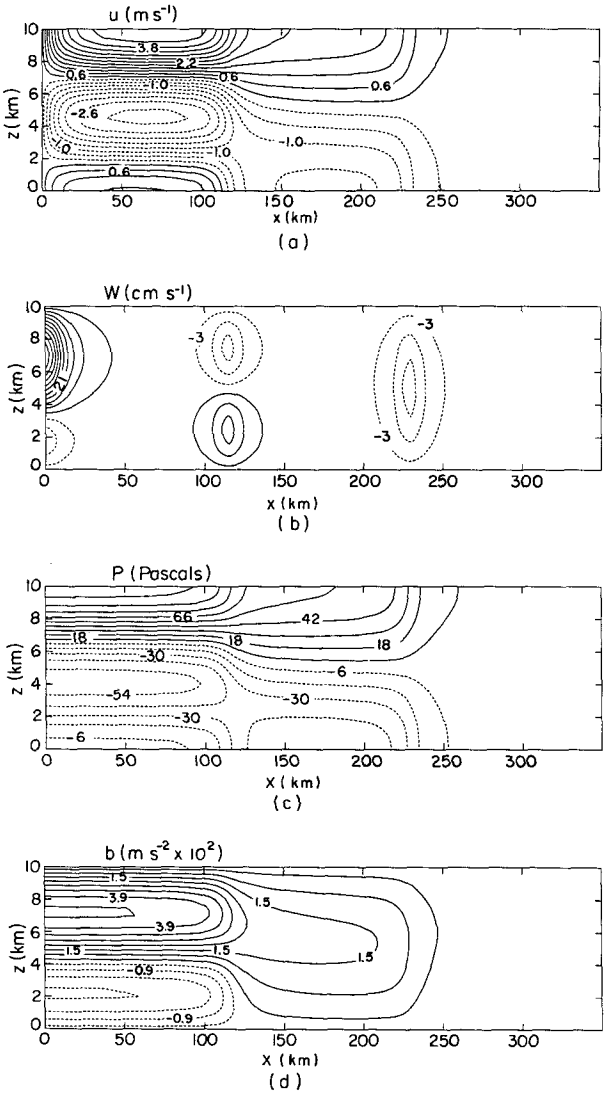

FIG. 5. Rigid-lid solution for superposition of $n = 1$ and 2 modes. The magnitude of Q_{m0} is 1.0 J kg^{-1} s^{-1}, $a = 10$ km, $H = 10$ km, $N = 0.01$ s^{-1} and $t = 2$ h. As in Fig. 3.

The fields of u, w, p, and b show some similarity to those that occur in both simulated and observed mesoscale convective systems. For example, Figs. 17, 18, and 19 of Nicholls (1987) show the early stages of the development of a numerically simulated tropical squall line that developed in a low-level jet. The basic pattern of the pressure field corresponds fairly well to the analytical solution (Fig. 5c). Observational studies of convective lines also indicate the presence of a surface mesohigh with surface mesolows on either side (Fujita 1963; Hoxit et al. 1976; Zipser 1977; Johnson and Nicholls 1983; Johnson and Hamilton 1988) and the existence of a mesolow above the surface mesohigh (LeMone 1983; LeMone et al. 1884). The analytic

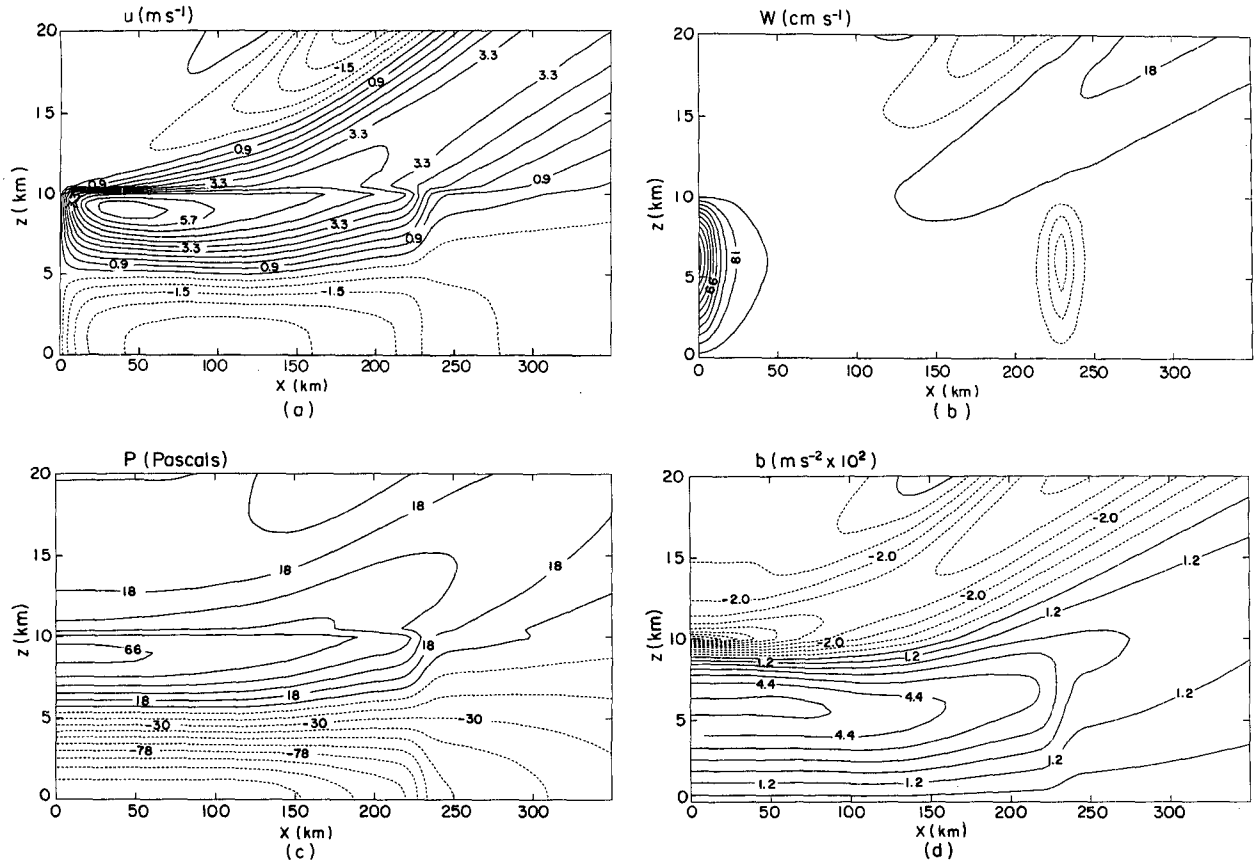

FIG. 6. Solution for a semi-infinite region. As in Fig. 3, except the contour intervals for u, w, and b are 0.6 m s^{-1}, 12 cm s^{-1}, and 0.008 m s^{-2}, respectively.

buoyancy field (Fig. 5d) does not show the density current that occurs in the Nicholls (1987) simulation but does portray the symmetrical regions of deep warming on either side of the convection. A noticeable difference is that the simulated squall line shows a tilted front-to-rear flowing updraft and rear-to-front flowing downdraft. However, the $n = 1$ modal response is clearly seen in the perturbation horizontal velocity field outside the convective region, which shows low-level flow towards the system and upper-level flow away. The simulated vertical velocity field shows subsidence at the leading edges of the deep warm regions. Vertically propagating gravity waves are evident in the numerical simulation and the convective-scale updraft mass flux appears to be balanced mainly by the convective-scale downdraft. Hence, for this case the main similarity between the numerical simulation and the analytic model is exterior to the convective region for which the $n = 1$ mode is the dominant response. The $n = 1$ modal response is also seen outside the region of active convection for the case of weak shear aloft simulated by Nicholls et al. (1988, Figs. 3 and 4). This system formed in an environment with moderate low-level shear and had a vertically oriented updraft for the first three hours of its lifetime. By two hours of simulation time the deep fast moving subsident warming regions had already exited the 300-km wide domain (Fig. 3d of that paper). Also noticeable in that simulation was that a waterloading effect significantly modified the pressure field within the precipitation shaft and a low-level warming occurred above the cold pool. The systems simulated by Nicholls et al. (1988) produced surface cold pools which are very likely highly nonlinear in character. Furthermore, the spatial distribution of the heating in those simulations was more complicated than for the analytic model discussed in this paper since the updraft is often tilted from the vertical.

The winter MONEX systems studied by Johnson and Kriete (1982) begin as clusters of cumulonimbus clouds but transformed into a mesoscale cloud system characterized by a large stratiform cloud layer. Figure 6 of Johnson and Kriete (1982) shows a system with midlevel inflow on either side of the system feeding upper and lower level downdrafts, which is a feature of the simple model presented here for the stratiform-type heating profile. Certain environments may be more likely to show the modal responses found for this simple model. The convective lines that form over the Florida peninsula usually occur in an environment that is only weakly sheared (e.g., Blanchard 1985) and they do not produce an extensive stratiform region. Hence, it might be expected that the $n = 1$ mode would be the

dominant response. The solution found for the stratiform-type heating profile ($n = 1$ and $n = 2$ mode combined) may be more applicable for rainbands forming in weakly sheared environments that have a deep layer of convectively unstable air (allowing midlevel air to enter the updraft circulation) and are not conducive to the formation of strong cold pools. The spatial distribution of the prescribed heating function is fixed. This may be reasonable for the convective region of a cloud line, but stratiform regions typically undergo a lengthy growing stage. Hence, the spatial distribution of heating can depend on the evolutionary stage of the convective line as well as environmental influences controlling the type of system that develops.

Although idealized, some interesting dynamical results emerge from this model. For a stratiform-type thermal forcing of fixed spatial extent, deep tropospheric subsidence warming occurs in response to the $n = 1$ component of heating, which rapidly propagates away from the system. A midlevel inflow develops in response to the $n = 2$ component of heating which grows outward from the source at half the speed of the $n = 1$ mode. Associated with this $n = 2$ mode is warming in the upper troposphere and cooling in the lower troposphere. This cool region also expands outward far beyond the strong source region due to adiabatic cooling produced by low-level compensating uplift, in much the same way as compensating subsidence causes warming to extend far beyond the strong heat source region for the $n = 1$ mode.

3. Solution for a semi-infinite region

Consider the case where heating is confined below H; then for a semi-infinite region the equations for perturbation pressure in transformed space become

$$\hat{p}_{zz} - \lambda^2 \hat{p} = \frac{Q_0 a e^{-ak}}{s^2} l \cos(lz), \quad \text{for} \quad z < H, \tag{18}$$

and

$$\hat{p}_{zz} - \lambda^2 \hat{p} = 0, \quad \text{for} \quad z > H. \tag{19}$$

The boundary condition at $z = \infty$ is assumed to be $\partial \hat{p}/\partial z = 0$. The solutions are

$$\hat{p} = A \cosh(\lambda z) - \frac{Q_0 a e^{-ak} l \cos(lz)}{s^2(\lambda^2 + l^2)}, \quad \text{for} \quad z < H, \tag{20}$$

and

$$\hat{p} = Be^{-\lambda z}, \quad \text{for} \quad z > H. \tag{21}$$

Requiring that p and $\partial p/\partial z$ are continuous at $z = H$, the constants A and B can be determined. We find

$$\hat{p} = \frac{Q_0 a e^{-ak}}{l}\left\{\frac{\cos(lH)}{2}\left[\frac{e^{kN(z-H)/s} + e^{-kN(z+H)/s}}{s^2 + (kN/l)^2}\right] - \frac{\cos(lz)}{l[s^2 + (kN/l)^2]}\right\}, \quad \text{for} \quad z < H, \tag{22}$$

and

$$\hat{p} = \frac{Q_0 a e^{-ak}}{l}\frac{\cos(lH)}{2}\left[\frac{e^{-kN(z+H)/s} - e^{-kN(z-H)/s}}{s^2 + (kN/l)^2}\right], \quad \text{for} \quad z > H. \tag{23}$$

Using the convolution integral, the inverse Laplace transform of Eq. (22) can be written:

$$\tilde{p}(k, z, t) = \frac{Q_0 a e^{-ak}}{l}\left\{\frac{\cos(lH)}{2}\int_0^t \cos\left[\frac{kN(t-\tau)}{l}\right]\cdot[J_0(2\sqrt{kN(H-z)\tau}) + J_0(2\sqrt{kN(H+z)}\cdot\tau)]d\tau - \frac{l}{kN}\cos(lz)\sin\left(\frac{kNt}{l}\right)\right\}, \quad \text{for} \quad z < H. \tag{24}$$

The inverse Fourier transform of Eq. (24) can be written

$$p(x, z, t) = \frac{-Q_0 a \cos(lz)}{N}\cdot\frac{1}{2}\left[\tan^{-1}\left(\frac{Nt/l + x}{a}\right) + \tan^{-1}\left(\frac{Nt/l - x}{a}\right)\right] + \frac{Q_0 a}{l}\frac{\cos(lH)}{2}\int_0^\infty e^{-ak} \times \left\{\int_0^t \cos\left[\frac{kN}{l}(t-\tau)\right]\cdot[J_0(2\sqrt{kN(H-z)\tau}) + J_0(2\sqrt{kN(H+z)\tau})]d\tau\right\}\cos(kx)dk, \quad \text{for} \quad z < H. \tag{25}$$

Similarly for $z > H$, we find,

$$p(x, z, t) = \frac{Q_0 a}{l}\frac{\cos(lH)}{2}\int_0^\infty e^{-ak}\left\{\int_0^t \cos\left[\frac{kN(t-\tau)}{l}\right]\cdot[J_0(2\sqrt{kN(H+z)\tau}) - J_0(2\sqrt{kN(H-z)\tau})]d\tau\right\}\cos(kx)dk, \quad \text{for} \quad z > H. \tag{26}$$

Solutions for the other variables are given in the Appendix. For $z < H$ they have the form of a sum of the rigid-lid solution and another part involving the zero-order Bessel function. The double integrals can be evaluated numerically using Simpson's rule and approximate expressions for the Bessel function.

If the anelastic continuity equation is used instead of the incompressible continuity equation, the equation for pressure is identical to Eq. (5). It is not necessary to consider ρ_0 a constant as long as it is understood that $\rho_0(z)Q(x, z)$ has the form given in Eq. (6). Therefore, the heating rate is weighted by the factor $1/\rho_0(z)$ compared to the case where ρ_0 is assumed constant. The variables u, w and b are also multiplied by a factor of $1/\rho_0(z)$. This complication is necessary since the solution for large z is required. The density variation with height is taken to be $\rho_0(z) = \rho_0(0)\exp(-z/H_s)$, where H_s is the scale height. A term

$$g\frac{c_v}{c_p}\frac{p'}{p_0}$$

has been neglected from the vertical equation of motion that should be retained for deep vertical scales (Dutton and Fichtl 1969). This approximation is made in order to obtain an analytic solution.

Figures 6a–d show u, w, p and b, respectively, at 2 h for $Q_{m0} = 2$ J kg^{-1} s^{-1} and the $n = 1$ mode. Comparing this figure with the rigid-lid case (Fig. 3), it can be seen that the structure of the response is very similar, in particular, close to the source region. Both solutions approach a steady state [satisfied by the time independent version of Eqs. (1)–(4)] in a region that broadens with time. A cool region develops above the heat source and upward-propagating gravity waves are present. Beneath the top of the heat source the magnitude of the compensating subsidence compared with the magnitude of the upward motion within the source region is considerably less than for the rigid-lid case. Furthermore, the compensating subsidence occurs over a broader region, although this is not evident from the figure due to the contour interval. This appears to be consistent with the upward propagation of energy and the necessity of balancing the upward mass flux within the heat source region. However, even after several hours the solution for the semi-infinite region still has many similarities with the rigid-lid case.

It is interesting to compare the upward propagation of gravity waves for the linear hydrostatic solution for constant N with that of a nonlinear, nonhydrostatic solution for a more realistic atmospheric environment. (Comparison was also made with a nonlinear, nonhydrostatic solution for constant N and reasonable agreement was found for moderate heating rates.) Figures 7a and 7b show the linear hydrostatic solution for vertical velocity and for $Q_{m0} = 2$ J kg^{-1} s^{-1}, $N = 0.01$ s^{-1}, $H = 5$ km, $a = 10$ km at $t = 1200$ s and 3600 s, respectively. Figures 8a and 8b show the numerical solution for the same heat source using the Colorado State University Modeling System (RAMS). The reader is referred to Nicholls et al. (1991) for a description of the model. This latter solution is nonlinear, nonhydrostatic and includes an eddy diffusion parameterization. The thermodynamic environment is a Florida summertime sounding (Nicholls et al. 1991, see Fig. 1). The horizontal resolution is 4 km and the vertical resolution is 500 m. The upper boundary con-

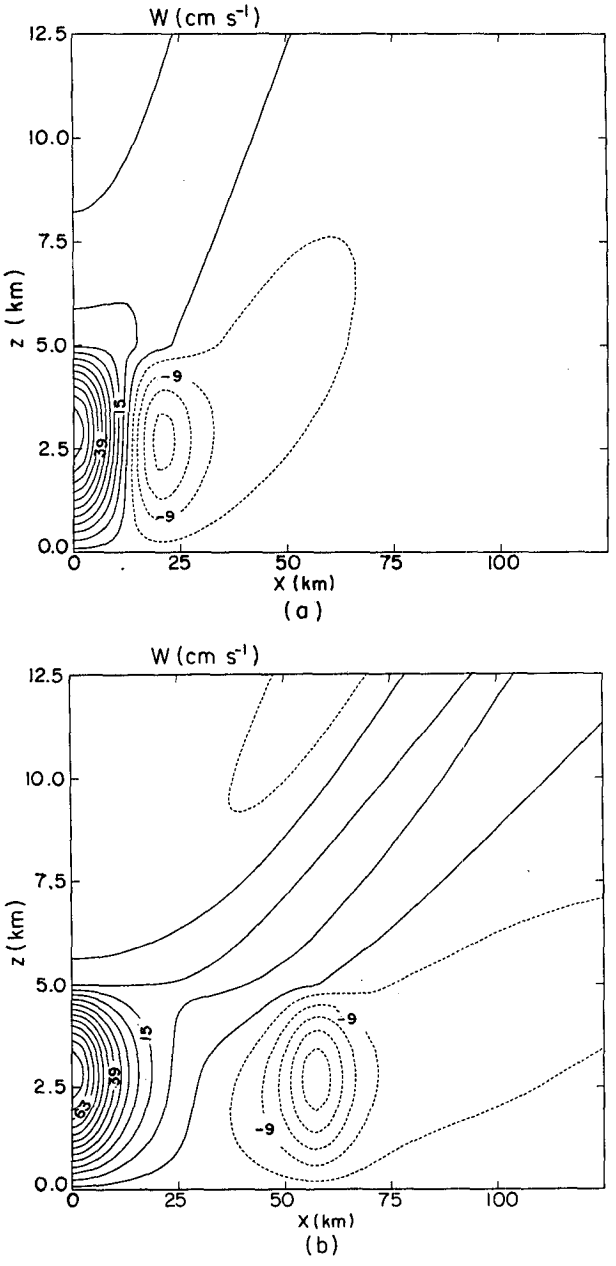

FIG. 7. Linear hydrostatic solution for a semi-infinite region for $n = 1$, $Q_{m0} = 2.0$ J kg^{-1} s^{-1}, $a = 10$ km, and $H = 5$ km. (a) Vertical velocity at 1200 s. (b) Vertical velocity at 3600 s. The contour interval is 0.06 m s^{-1}.

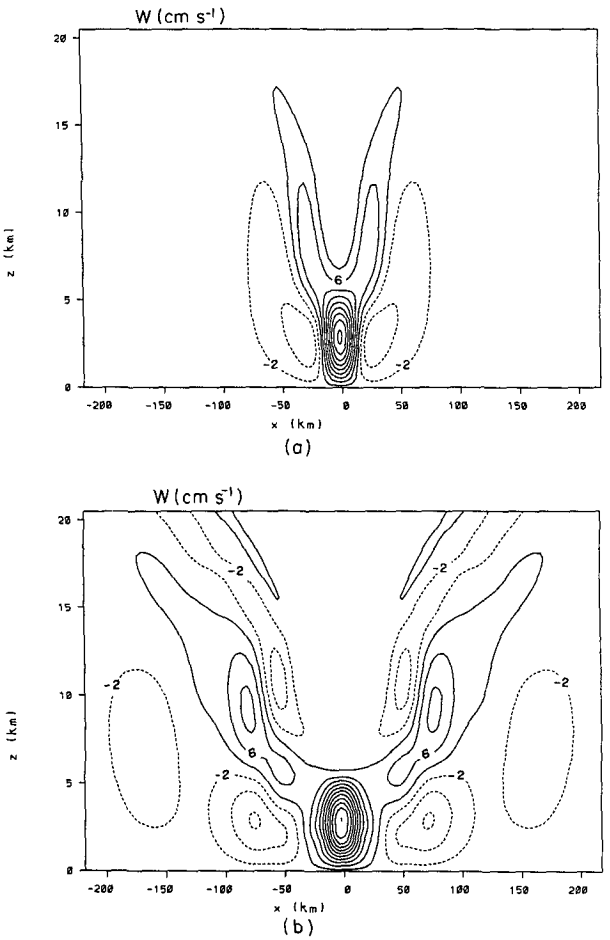

FIG. 8. Numerical simulation for the same heating function as in Fig. 7. (a) Vertical velocity at 1200 s. (b) Vertical velocity at 3600 s. The contour interval is 0.04 m s^{-1}.

dition at $z = 28$ km is a rigid lid. A weak dissipative layer 5 km in depth is included at the top of the domain to reduce reflection of gravity waves from the upper boundary.

The linear hydrostatic solution shows a region of upward motion extending in a jetlike flow from the top of the heat source. This upward motion, which is evidently a wave front, began with an almost vertical orientation and tilted with time. The downward propagation of phase lines with time indicates an upward propagation of wave energy. The center of the compensating subsidence moves from $x = 20$ km at 1200 s to $x = 60$ km at 3600 s. Regions of weak downward motion occur both behind and ahead of the jetlike upward directed flow. The numerical simulation at $t = 1200$ s (Fig. 8a) shows a similar upward motion occurring in a jetlike flow on either side of the heat source (note that the magnitudes are not the same since w is very sensitive to N which varies from ~ 0.012 s^{-1} in the lower troposphere to ~ 0.009 s^{-1} in the upper troposphere). However, the upward motion appears to be more vertically oriented in the upper troposphere. Above the tropopause at 13.5 km the wave front becomes more tilted. Comparison of the linear hydrostatic solution with the numerical simulation at $t = 3600$ s shows some significant differences. The main region of upward motion slanting away from the top of the heat source is apparent for both solutions. However, significant reflection is occurring at the tropopause where there is an abrupt change in stability. It seems as if the source is being projected onto the natural harmonics that occur between the surface and the tropopause. For instance, downward motion occurs at $x = \pm 160$ km corresponding to an $n = 1$ mode for a rigid-lid solution and $H = 13.5$ km. The compensating subsidence seen in the linear hydrostatic solution at $x \sim 60$ km is also seen in the numerical model. However, above this occurs strong upward motion, and this is like an $n = 2$ mode. Trailing this at $x = 40$ km is a slower moving $n = 3$ mode. As time goes on, more wave fronts become evident above the heat source. Interestingly, the solution not only reaches a steady state in a continuously expanding region beneath the top of the heat source, but also above it, where an everwidening undisturbed region forms. The regions where compensating subsidence occurs outside the heat source in Fig. 8b is evidently dependent to some extent on the partially trapped gravity wave modes.

It is reasonable to conclude that a significant fraction of the gravity wave energy is trapped by the change in stability at the tropopause, but further investigation is required to determine the actual amount. A detailed analysis of the upward propagation of gravity wave energy is beyond the scope of this study. The effects of vertically varying buoyancy frequency and wind shear on the structure and propagation of gravity waves are discussed by Lindzen and Tung (1976), Tripoli and Cotton (1989a,b), Crook (1988), Schmidt and Cotton (1990), and others.

A numerical simulation was also carried out for a stronger heat source having a smaller horizontal scale ($a = 4$ km), which led to vertical velocities in excess of 10 m s^{-1}. Nonlinear terms become important in this case. Nevertheless, comparison with an identical simulation but for a much reduced heat source showed that the wave fronts away from the source had the same phase.

Simulations by Schmidt and Cotton (1990) developed flattened layers of lower stratospheric cooling and upper tropospheric warming. The linear hydrostatic solution for the buoyancy field at $t = 7200$ s (Fig. 6d) also shows a flattened layer of cooling above the level of the heat source. This cooling develops due to upward motion in the jetlike flow which tilts with time. Figures 6b and 7b indicate that downward motion occurs behind the upward motion at upper levels which prevents a persistent cool region developing aloft. However, just above the level of the heat source downward motion

does not occur behind the region of upward motion. Mass balance is achieved by large-scale weak subsidence ahead of the region of upward motion. The magnitude of the cooling that develops just above the heat source is larger than the warming beneath. Johnson and Kriete (1982) in an observational study of Borneo systems found significant cooling in the lower stratosphere. The results presented here show that linear dynamics can produce cooling above the level of the heat source and that this can be significant even for a constant N.

If a cooling rate is applied between the surface and $z = 5$ km, then the solution is the same as in Figs. 7 and 8, except the signs of the vertical velocities are reversed. A strong cooling rate that extends to the surface will create a density current for which nonlinearities are important. Nevertheless, the partially trapped linear modes are still forced. They appear to be an important component of the response to low level cooling and require further investigation.

4. Solution for a pulse forcing

Consider a pulse forcing for which the heating is turned off after some interval T. The solution for a rigid lid can be shown to be

$$p(x, z, t) = \frac{-Q_0 a \cos(lz)}{N} \cdot \frac{1}{2}\left\{\tan^{-1}\left[\frac{N(T+t')/l + x}{a}\right] + \tan^{-1}\left[\frac{N(T+t')/l - x}{a}\right] - \tan^{-1}\left(\frac{x + Nt'/l}{a}\right) + \tan^{-1}\left(\frac{x - Nt'/l}{a}\right)\right\}. \quad (27)$$

$$b(x, z, t) = \frac{Q_0 a l \sin(lz)}{N} \cdot \frac{1}{2}\left\{\tan^{-1}\left[\frac{N(T+t')/l + x}{a}\right] + \tan^{-1}\left[\frac{N(T+t')/l - x}{a}\right] - \tan^{-1}\left(\frac{x + Nt'/l}{a}\right) + \tan^{-1}\left(\frac{x - Nt'/l}{a}\right)\right\}. \quad (28)$$

$$w(x, z, t) = \frac{-Q_0 \sin(lz)}{N^2} \cdot \frac{1}{2}\left\{\frac{1}{1 + \left[\frac{N(T+t')/l + x}{a}\right]^2} + \frac{1}{1 + \left[\frac{N(T+t')/l - x}{a}\right]^2} - \frac{1}{1 + \left[\frac{x + Nt'/l}{a}\right]^2} - \frac{1}{1 + \left[\frac{x - Nt'/l}{a}\right]^2}\right\}. \quad (29)$$

$$u(x, z, t) = \frac{Q_0 a l}{N^2} \cos(lz) \frac{1}{2}\left\{\tan^{-1}\left[\frac{N(T+t')/l + x}{a}\right] - \tan^{-1}\left[\frac{N(T+t')/l - x}{a}\right] - \tan^{-1}\left[\frac{x + Nt'/l}{a}\right] - \tan^{-1}\left[\frac{x - Nt'/l}{a}\right]\right\} \quad (30)$$

where t' is measured from the instant the forcing is switched off (i.e., $t' = t - T$). Before the heating is turned off, the solution is given by Eqs. (12)–(15). The arctangent form of the solution for perturbation pressure (or buoyancy) is sketched in Fig. 9. It consists of the two dashed curves which are a result of the earlier

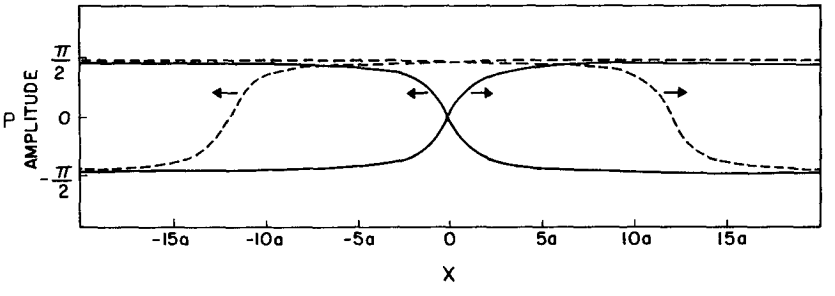

FIG. 9. Arctangent form of solution for a pulse forcing (see text for explanation).

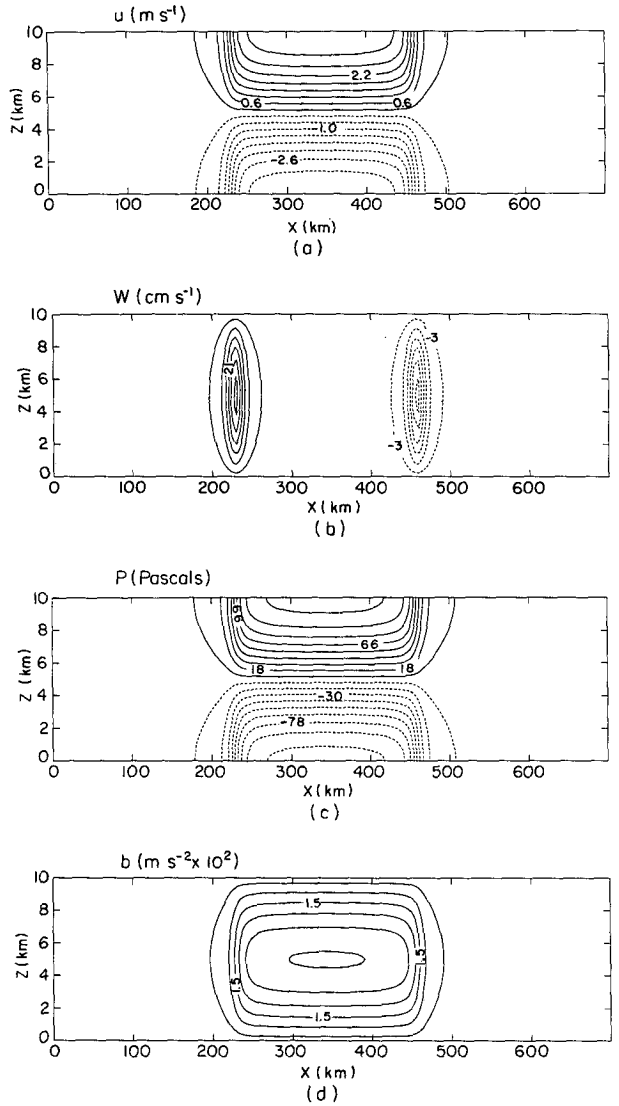

FIG. 10. Solution for a pulse forcing. As in Fig. 3, $T = 2$ h and $t' = 2$ h.

forcing and the two solid curves which negate one another at $t' = 0$, then subsequently move in the direction indicated by arrows. As they move apart, the two solid curves sum in the center canceling the perturbation produced by the dashed curves, leading to an undisturbed region that broadens with time. The solid and dashed curves move at the same speed producing two disturbances traveling in opposite directions, similar to the solution for the perturbed shallow water equations (see for instance, Gill 1982).

Figures 10a–d show fields of u, w, p and b, respectively, for the same $n = 1$ heating profile used previously (see Fig. 3), for $T = 2$ h and $t' = 2$ h (i.e., the heating is turned off at 2 h and these are the fields 2 h later). The disturbance has separated into two parts moving in opposite directions, leaving an undisturbed state in the region which was initially forced.

The disturbance is a clockwise rotating roll. At the leading edge, downward motion produces adiabatic warming, whereas at the back edge, upward motion leads to adiabatic cooling. A positive pressure perturbation exists aloft with a negative pressure perturbation at low levels. The propagation speed of the disturbance is NH/π. If higher-order slower moving modes are forced, the $n = 1$ mode will separate from them.

This solution can also be used to build expressions for a heating rate that is turned on at $t > 0$ or for a series of pulses. For instance, if a negative pulse starting at $t = 0$ is added to the solution for a positive pulse of equal magnitude but of longer duration, a pulse starting at a later time is obtained. In the next section we discuss a gravity wave produced in a two-dimensional simulation of Florida convection which has a similar structure to the solution found for a pulse forcing.

5. Term analysis of a numerically simulated gravity wave

Simulations of convection over the Florida peninsula were made using the Colorado State University Regional Atmospheric Modeling System (RAMS). Details of the model and simulations are presented in Nicholls et al. (1991). During the morning, sea-breeze circulations develop and move inland. By the early afternoon, deep convection starts to develop at the sea-breeze fronts. The strongest convection occurs during the late afternoon as the sea-breeze fronts converge. The subsequent decay of this strong convection produces two deep, oppositely moving, gravity waves.

Figures 11a–d show fields of horizontal velocity, vertical velocity, perturbation pressure, and perturbation temperature, respectively, in the region of one of these waves. The gravity wave is moving from left to right and was generated two and a half hours earlier. It has the structure of a clockwise rotating roll. The central region is warm and a high-pressure perturbation exists aloft with a low-pressure perturbation near the surface. Downward motion at the leading edge produces adiabatic warming, whereas upward motion at the back edge leads to adiabatic cooling.

In order to compare the numerical model results with those of the analytical model, the simulated fields are analyzed in terms of the Boussinesq equations:

$$\frac{\partial u}{\partial t} + \frac{1}{\rho_0}\frac{\partial p'}{\partial x} = -u\frac{\partial u}{\partial x} - w\frac{\partial u}{\partial z} \tag{31}$$

$$\frac{1}{\rho_0}\frac{\partial p'}{\partial z} - g\frac{\theta'}{\theta_0} = -\frac{\partial w}{\partial t} - u\frac{\partial w}{\partial x} - w\frac{\partial w}{\partial z} + g(0.61q_v' - q_l) \tag{32}$$

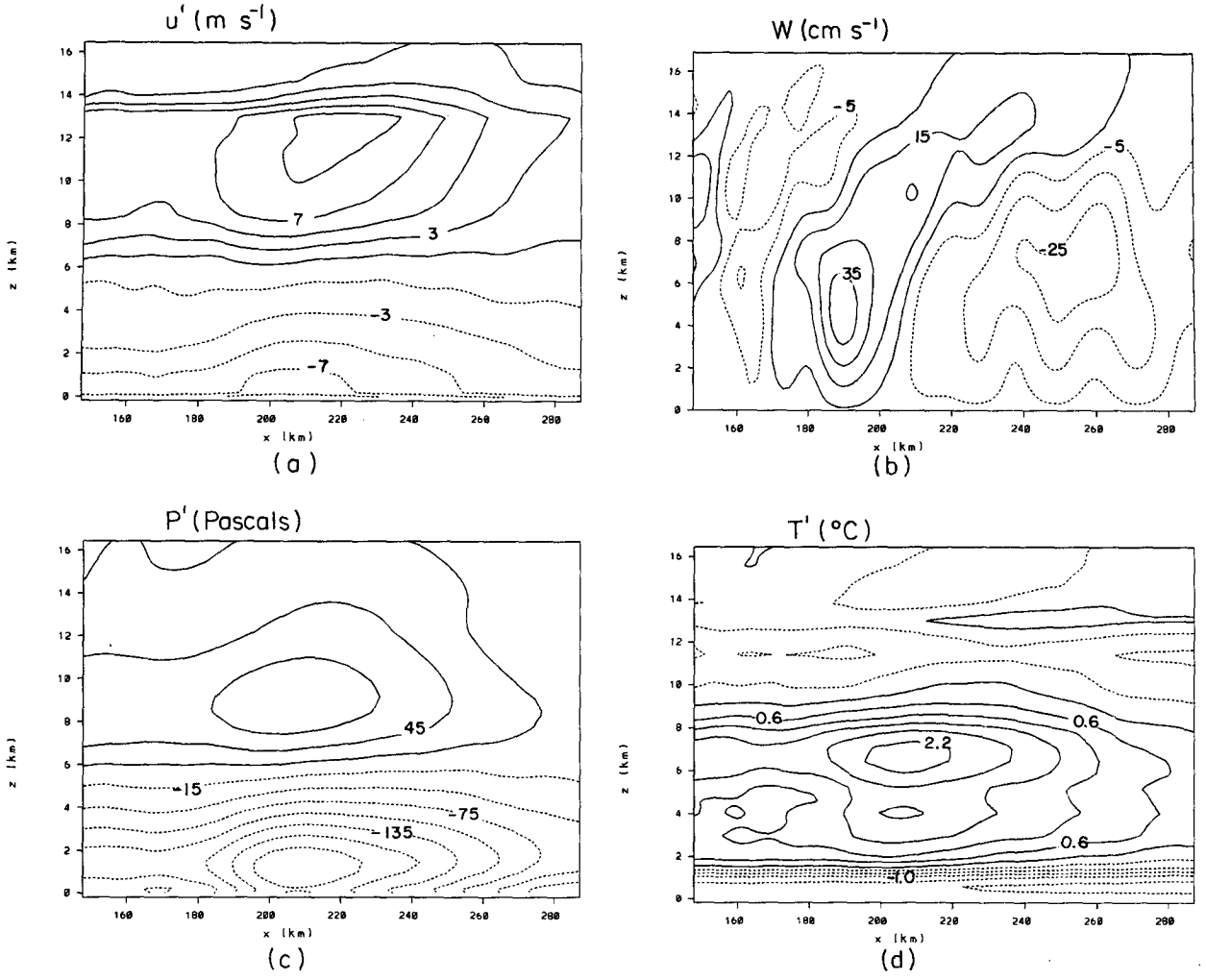

FIG. 11. Gravity wave produced in a numerical simulation of Florida convection. (a) Horizontal velocity perturbation from the initial state. The contour interval is 2 m s^{-1}. (b) Vertical velocity. The contour interval is 10 cm s^{-1}. (c) Perturbation pressure. The contour interval is 0.3 mb. (d) Perturbation temperature. The contour interval is 0.4°C.

$$\frac{\partial}{\partial t}\left(g\frac{\theta'}{\theta_0}\right) + wN^2 = Q - u\frac{\partial}{\partial x}\left(g\frac{\theta'}{\theta_0}\right) - w\frac{\partial}{\partial z}\left(g\frac{\theta'}{\theta_0}\right) \tag{33}$$

$$\frac{\partial}{\partial x}(\rho_0 u) + \frac{\partial}{\partial z}(\rho_0 w) = 0 \tag{34}$$

where θ' is the perturbation potential temperature, q'_v is the perturbation water vapor mixing ratio, and q_l is the liquid water mixing ratio. The terms on the left of these equations are linear terms for which we have derived analytical solutions for a prescribed heating function. In order to verify that the simulated gravity wave is approximately linear a term analysis is carried out. Figures 12a–d show results for the four terms in the horizontal momentum equation for the gravity wave shown in Fig. 11. It can be seen that the balance is predominantly one between the local change of u and the horizontal gradient of the perturbation pressure. A term analysis for the other equations shows the disturbance is nearly in hydrostatic balance and that for the thermodynamic equation, the balance is between the local change in buoyancy and wN^2. Hence, the nonlinear terms are relatively small (the magnitude of the subgrid-scale turbulence terms used in the numerical simulation are also small).

Within the convective region nonlinear terms are significant. Nevertheless, the linear terms have a broad similarity to what they would be in the absence of nonlinear effects and are usually slightly larger in magnitude than the nonlinear terms (not shown). Figure 13 shows the time variation of the net heating occurring in the convective region during the formative stage of the gravity wave. There is a large peak at 1630 EST

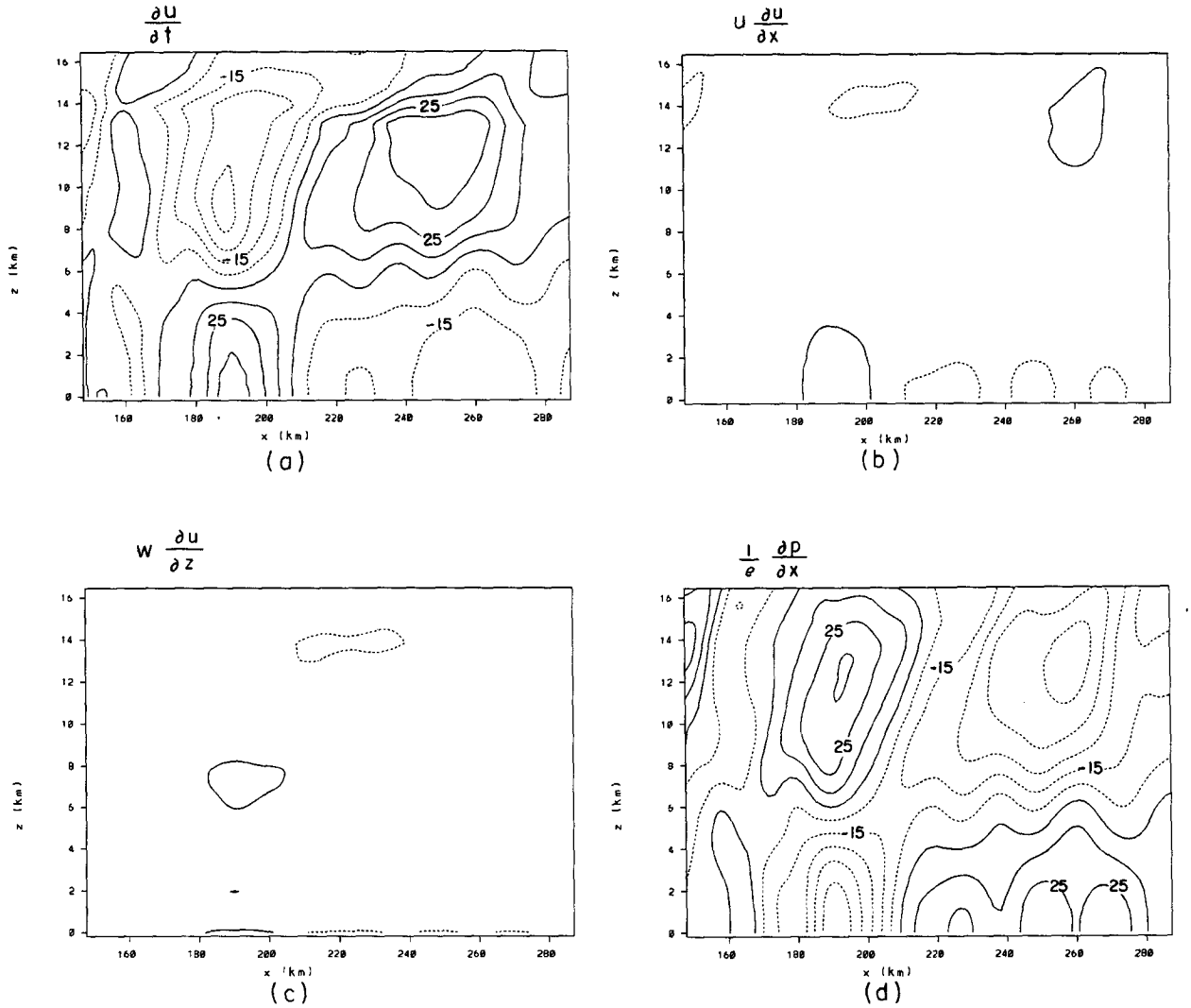

FIG. 12. Term analysis of the horizontal momentum equation. (a) $\partial u/\partial t$, (b) $u(\partial u/\partial x)$, (c) $w(\partial u/\partial z)$, (d) $\rho^{-1}(\partial p/\partial x)$. The contour interval is 0.001 m s^{-1} and the label scale 10^4.

followed by a secondary peak at 1700 EST. The first peak occurred when the sea-breeze fronts converged and a cumulus convective cell explosively developed. The cell then decayed in intensity which was apparently associated with the fallout of precipitation into the updraft. It was at this stage that the two oppositely moving gravity waves formed. The collapse of this cell is evident in the sharp decrease in the heating rate that occurs at 1640 EST.

Equations (31)–(34) can be combined into an equation for the perturbation pressure:

$$\frac{\partial^2}{\partial t^2} p'_{zz} + N^2 p_{xx} = \frac{\partial}{\partial t}\frac{\partial}{\partial z}\left(\rho_0 Q - \frac{\partial B}{\partial t} - C\right) - N^2 \frac{\partial A}{\partial x} \tag{35}$$

where

$$\frac{A}{\rho_0} = u\frac{\partial u}{\partial x} + w\frac{\partial u}{\partial z}$$

$$\frac{B}{\rho_0} = \frac{\partial w}{\partial t} + u\frac{\partial w}{\partial x} + w\frac{\partial w}{\partial z} + g(0.61q'_v - q_l)$$

$$\frac{C}{\rho_0} = u\frac{\partial}{\partial x}\left(g\frac{\theta'}{\theta_0}\right) + w\frac{\partial}{\partial z}\left(g\frac{\theta'}{\theta_0}\right).$$

This equation is identical to Eq. (5) if $A = B = C = 0$. The additional terms are only large within the region of strong convection, so it appears that $\partial B/\partial t$ and C could be considered as resulting in a modified source term acting on the far field. A similar interpretation is made by Raymond (1983). However, since

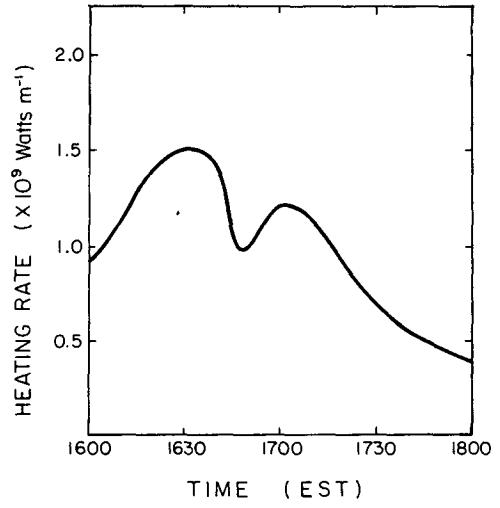

FIG. 13. Time variation of net heating within the convective region.

the term involving A is not within the same derivatives as Q, its effect is likely to be more complicated. The effects of vertical transports of horizontal momentum enter through this term so it might be associated with an asymmetrical response such as seen in many squall lines where there is a front-to-rear flowing updraft and a rear-to-front flowing downdraft. Nevertheless, there is clearly a similarity between the gravity wave produced in the numerical simulation of Florida convection and the analytic solution for the pulse forcing.

There is evidence of a less well-defined wave trailing the main gravity wave. For instance, there is downward motion at $x = 165$ km in Fig. 11b. This may be caused by the second heating peak (Fig. 13). It is not necessary that the downward mass flux within the first gravity wave should balance the upward mass flux at its back edge, since it may be partly compensating for upward motion within the source region. Certainly, the heating rate shown in Fig. 13 does not decrease to zero when the wave forms but only to two-thirds of the peak value. For this two-dimensional simulation, compensating subsidence does not simply occur uniformly over a broad region. It occurs in certain regions within a train of gravity waves that are forced by cellular convection. The magnitude of the downward motion within the main gravity wave (Fig. 11b) is less than the upward motion at the back edge. However, it occurs over a broader region. This structure may be a result of gravity wave energy escaping upwards as discussed in section 3.

6. Conclusions

In this paper, a simple model of the forced gravity wave response to prescribed heat sources and sinks is developed. The main conclusions are: 1) although the model is linear, it reproduces some of the features observed in mesoscale convective lines; 2) the response propagates away from the source with a speed that depends on the Brunt–Väisälä frequency and the vertical wavenumber of the heating; 3) as the wave front propagates past a region, the fields of u, p, and b initially increase rapidly and then slowly approach a constant value; and 4) two modes appear to be of particular interest. The $n = 1$ mode which is deep and fast moving (~ 30 m s^{-1}) produces subsidence warming at large distances from the source. The scale of the subsidence depends on the half-width of the heating and can be concentrated in a fairly narrow region. The $n = 2$ mode, which is slower moving (~ 15 m s^{-1}), is associated with midlevel inflow and upper and lower level outflows; 5) for a semi-infinite region, although gravity wave energy can propagate upwards, the solution still shows a marked resemblance to the rigid-lid solution; 6) significant trapping of wave energy is produced by the change in stability at the tropopause; 7) the results of this linear two-dimensional model suggest that when systems decay there is not an overshooting in the updraft region followed by a subsequent rebound. Nor is upward motion forced by convergence into the broad surface mesolows on either side of the system. As in the case of the perturbed shallow water equations, the disturbance separates into two parts moving in opposite directions; 8) the traveling disturbances caused by a sudden decrease in the forcing have a roll-like structure and are similar to the gravity waves produced in a two-dimensional numerical simulation of Florida convection; and 9) a term analysis of the simulated gravity wave confirms it is predominantly linear in character.

The rapid extension of the surface mesolows on either side of a simulated squall line was noted by Nicholls (1987). The effect of the $n = 1$ mode, outside the region influenced by the $n = 2$ mode, is to create a broad region of rather uniform low surface pressure which builds quickly away from the forcing region. The pressure field can be decomposed into partial pressures from buoyant and dynamic contributions in the manner described by Rotunno and Klemp (1982). In the model presented in this article, dynamic terms that arise from the inclusion of nonlinear advective effects have been omitted. Dynamic terms become important in regions where there is strong shear and large vertical motions (Rotunno and Klemp 1982; Schlesinger 1984; LeMone et al. 1988; Nicholls et al. 1988).

The studies by Lin and Goff (1988), and Bosart and Seimon (1988) of persistent large-amplitude gravity waves suggest that they were initiated by convective systems. The results of this study may be relevant to this initiation mechanism. The analysis of Lin and Goff (1988) indicated that the disturbance they observed was a type of solitary wave (or soliton) that propagates along an inversion for which nonlinear and dispersive effects are predominant, unlike the linear gravity waves obtained in this study.

Clearly there are limitations to a model that is linear, hydrostatic, uses prescribed forcing, and which has a nonsheared motionless initial state. However, it does shed light on a number of features that have been observed and simulated by more complex models. It also provides a foundation for the study of the energetics of thermally forced gravity waves. We are currently investigating how much of the latent heat energy released in thunderstorms is propagated away by this type of gravity wave.

Acknowledgments. Discussions with Jerome Schmidt, Dr. Wayne Schubert, and Piotr Flatau are appreciated. Thanks to Tony Smith, Bryan Critchfield, and Dallas McDonald for preparing this manuscript. This research was supported by the National Science Foundation Grants ATM-86 16662, ATM-89 15265, and ATM-88 14913. Acknowledgement is made to the National Center for Atmospheric Research, which is sponsored by the National Science Foundation, for the computing time used in this research.

APPENDIX

Semi-infinite solution for the perturbation buoyancy, vertical velocity, and horizontal velocity:

$$b(x, z, t) = \frac{Q_0 a l \sin(lz)}{N} \cdot \frac{1}{2}\left[\tan^{-1}\left(\frac{Nt/l + x}{a}\right) + \tan^{-1}\left(\frac{Nt/l - x}{a}\right)\right] + \frac{Q_0 a \cos(lH)}{2} \int_0^\infty e^{-ak} \times \left\{\int_0^t \sin\left[\frac{kN}{l}(t-\tau)\right] \cdot [J_0(2\sqrt{kN(H-z)\tau}) - J_0(2\sqrt{kN(H+z)\tau})]d\tau\right\} \cos(kx)dk, \quad \text{for} \quad z < H. \quad \text{(A1)}$$

$$b(x, z, t) = \frac{Q_0 a \cos(lH)}{2} \int_0^\infty e^{-ak}\left\{\int_0^t \sin\left[\frac{kN}{l}(t-\tau)\right] \times [J_0(2\sqrt{kN(H-z)\tau}) - J_0(2\sqrt{kN(H+z)\tau})]d\tau\right\} \times \cos(kx)dk, \quad \text{for} \quad z > H. \quad \text{(A2)}$$

$$w(x, z, t) = \frac{Q_0 \sin(lz)}{N^2}\left\{\frac{a^2}{x^2 + a^2} - \frac{1}{2}\left[\frac{1}{1 + \left(\frac{Nt/l + x}{a}\right)^2} + \frac{1}{1 + \left(\frac{Nt/l - x}{a}\right)^2}\right]\right\} - \frac{Q_0 a \cos(lH)}{2Nl} \int_0^\infty e^{-ak} \cdot k\left\{\int_0^t \cos\left[\frac{kN}{l}(t-\tau)\right] \times [J_0(2\sqrt{kN(H-z)\tau}) - J_0(2\sqrt{kN(H+z)\tau})]d\tau\right\} \times \cos(kx)dk, \quad \text{for} \quad z < H. \quad \text{(A3)}$$

$$w(x, z, t) = \frac{-Q_0 a \cos(lH)}{2Nl} \int_0^\infty e^{-ak} k\left\{\int_0^t \cos\left[\frac{kN}{l}(t-\tau)\right] \times [J_0(2\sqrt{kN(H-z)\tau}) - J_0(2\sqrt{kN(H+z)\tau})]d\tau\right\} \times \cos(kx)dk, \quad \text{for} \quad z > H. \quad \text{(A4)}$$

$$u(x, z, t) = \frac{Q_0 a l \cos(lz)}{N^2} \cdot \frac{1}{2}\left[\tan^{-1}\left(\frac{Nt/l + x}{a}\right) - \tan\left(\frac{Nt/l - x}{a}\right) - \tan^{-1}\left(\frac{x}{a}\right)\right] + \frac{Q_0 a \cos(lH)}{2N} \int_0^\infty e^{-ak}\left\{\int_0^t \sin\left[\frac{kN}{l}(t-\tau)\right] \times [J_0(2\sqrt{kN(H-z)\tau}) + J_0(2\sqrt{kN(H+z)\tau})]d\tau\right\} \times \sin(kx)dk, \quad \text{for} \quad z < H. \quad \text{(A5)}$$

$$u(x, z, t) = \frac{Q_0 a \cos(lH)}{2N} \int_0^\infty e^{-ak}\left\{\int_0^t \sin\left[\frac{kN}{l}(t-\tau)\right] \times [-J_0(2\sqrt{kN(H-z)\tau}) + J_0(2\sqrt{kN(H+z)\tau})]\right\} \times \sin(kx)dk, \quad \text{for} \quad z < H. \quad \text{(A6)}$$

REFERENCES

Barnes, G. M., and K. Sieckman, 1984: The environment of fast- and slow-moving tropical mesoscale convective cloud lines. *Mon. Wea. Rev.*, **112**, 1782–1794.

Blanchard, D. O., and R. E. López, 1985: Spatial patterns of convection in South Florida. *Mon. Wea. Rev.*, **113**, 1282–1299.

Bosart, L. F., and A. Seimon, 1988: A case study of an unusually intense atmospheric gravity wave. *Mon. Wea. Rev.*, **116**, 1857–1886.

Bretherton, C. S., 1988: Group velocity and the linear response of stratified fluids to internal heat or mass sources. *J. Atmos. Sci.*, **45**, 81–93.

——, and P. K. Smolarkiewicz, 1989: Gravity waves, compensating subsidence, and detrainment around cumulus clouds. *J. Atmos. Sci.*, **46**, 740–759.

Crook, N. A., 1988: Trapping of low-level interval gravity waves. *J. Atmos. Sci.*, **45**, 1533–1541.

Dudhia, J., M. W. Moncrieff and D. W. K. So, 1987: The two-dimensional dynamics of west African squall lines. *Quart. J. Roy. Meteor. Soc.*, **113**, 121–146.

Dutton, J. A., and G. H. Fichtl, 1969: Approximate equations of motion for gases and liquids. *J. Atmos. Sci.*, **26,** 241–254.

Fujita, T., 1963: Analytical mesometeorology: A review. *Severe Local Storms, Meteor. Monogr.*, No. 27, Amer. Meteor. Soc., 77–125.

Garstang, M., P. D. Tyson and G. D. Emmitt, 1975: The structure of heat islands. *Rev. Geophys. Space Phys.*, **13,** 139–165.

Geisler, J. E., and F. P. Bretherton, 1969: The sea-breeze forerunner. *J. Atmos. Sci.*, **26,** 82–95.

Gill, A. E., 1980: Some simple solutions for heat-induced tropical circulation. *Quart. J. Roy. Meteor. Soc.*, **106,** 447–462.

——, 1982: *Atmosphere-Ocean Dynamics.* Academic Press, International Geophysics Series, **30,** Chapter 5.

Hane, C., 1973: The squall line thunder storm: Numerical experimentation. *J. Atmos. Sci.*, **30,** 1672–1690.

Houze, R. A., Jr., 1982: Cloud clusters and large-scale vertical motions in the tropics. *J. Meteor. Soc. Japan.*, **60,** 396–410.

Hoxit, L. R., C. F. Chappell and J. M. Fritsch, 1976: Formation of mesolows or pressure troughs in advance of cumulonimbus clouds. *Mon. Wea. Rev.*, **104,** 1419–1428.

Johnson, R. H., and D. C. Kriete, 1982: Thermodynamic and circulation characteristics of winter monsoon tropical mesoscale convection. *Mon. Wea. Rev.*, **110,** 1898–1911.

——, and M. E. Nicholls, 1983: A composite analysis of the boundary layer accompanying a tropical squall line. *Mon. Wea. Rev.*, **111,** 308–319.

——, and G. S. Young, 1983: Heat and moisture budgets of tropical mesoscale anvil clouds. *J. Atmos. Sci.*, **40,** 2138–2147.

——, and P. J. Hamilton, 1988: The relationship of surface pressure features to the precipitation and air flow structure of an intense midlatitude squall line. *Mon. Wea. Rev.*, **116,** 1444–1472.

LeMone, M. A., 1983: Momentum flux by a line of cumulonimbus. *J. Atmos. Sci.*, **40,** 1815–1834.

——, G. M. Barnes and E. J. Zipser, 1984: Momentum flux by lines of cumulonimbus over the tropical oceans. *J. Atmos. Sci.*, **41,** 1914–1932.

——, ——, J. C. Frankhauser and L. F. Tarleton, 1988: Perturbation pressure fields measured by aircraft around the cloud-base updraft of deep convective clouds. *Mon. Wea. Rev.*, **116,** 313–327.

Lin, Y. L., and R. B. Smith, 1986: Transient dynamics of airflow near a local heat source. *J. Atmos. Sci.*, **43,** 40–49.

——, and R. C. Goff, 1988: A Study of a mesoscale solitary wave in the atmosphere originating near a region of deep convection. *J. Atmos. Sci.*, **45,** 194–205.

——, and NS A. Li, 1988: Three-dimensional response of a shear flow to elevated heating. *J. Atmos. Sci.*, **45,** 2987–3002.

Lindzen, R. S., and K. K. Tung, 1976: Banded convective activity and ducted gravity waves. *Mon. Wea. Rev.*, **104,** 1602–1617.

Mahrer, Y., and R. A. Pielke, 1976: Numerical simulation of the airflow over Barbados. *Mon. Wea. Rev.*, **104,** 1392–1402.

Nicholls, M. E., 1987: A comparison of the results of a two-dimensional numerical simulation of a tropical squall line with observations. *Mon. Wea. Rev.*, **115,** 3055–3077.

——, R. H. Johnson and W. R. Cotton, 1988: The sensitivity of two-dimensional simulations of tropical squall lines to environmental profiles. *J. Atmos. Sci.*, **45,** 3625–3649.

——, R. A. Pielke and W. R. Cotton, 1991: A two-dimensional numerical investigation of the interaction between sea-breezes and deep convection over the Florida peninsula. *Mon. Wea. Rev.*, **119,** 298–323.

Raymond, D. J., 1983: Wave-CISK in mass flux form. *J. Atmos. Sci.*, **40,** 2561–2572.

——, 1986: Prescribed heating of a stratified atmosphere as a model for moist convection. *J. Atmos. Sci.*, **43,** 1101–1111.

Rotunno, R., and J. B. Klemp, 1982: The influence of the shear-induced pressure gradients on thunderstorm motion. *Mon. Wea. Rev.*, **110,** 136–151.

——, —— and M. L. Weisman, 1988: A theory for strong, long-lived squall lines. *J. Atmos. Sci.*, **45,** 463–485.

Schlesinger, R. E., 1984: Effects of the pressure perturbation field in numerical models of unidirectionally sheared thunderstorm convection: Two versus three dimensions. *J. Atmos. Sci.*, **41,** 1571–1587.

Schmidt, J. M., and W. R. Cotton, 1990: Interactions between upper and lower atmospheric gravity waves on squall line structure and maintenance. *J. Atmos. Sci.*, **47,** 1205–1222.

Smull, B. F., and R. A. Houze, 1987: Rear inflow in squall lines with trailing stratiform precipitation. *Mon. Wea. Rev.*, **115,** 2869–2889.

Thorpe, A. J., M. J. Miller and M. W. Moncrieff, 1982: Two-dimensional convection in nonconstant shear: A model of midlatitude squall lines. *Quart. J. Roy. Meteor. Soc.*, **108,** 739–762.

Tripoli, G. L., and W. R. Cotton, 1989a: Numerical study of an observed orogenic mesoscale convective system. Part I: Simulated genesis and comparison with observations. *Mon. Wea. Rev.*, **117,** 273–304.

——, and ——, 1989b: Numerical study of an observed orogenic mesoscale convective system. Part II: Analysis of governing dynamics. *Mon. Wea. Rev.*, **117,** 305–328.

Yanai, M., S. Structure and J. H. Chu, 1973: Determination of bulk properties of tropical cloud clusters from large-scale heat and moisture budgets. *J. Atmos. Sci.*, **30,** 611–627.

Zipser, E. J., 1977: Mesoscale and convective-scale downdrafts as distinct components of squall-line structure. *Mon. Wea. Rev.*, **105,** 1568–1589.